Applied Physics A (2023) 129:824
https://doi.org/10.1007/s00339-023-07050-w

Applied Physics A
Materials Science & Processing

Influence of water layer thickness on crater volume for nanosecond pulsed laser ablation of stainless steel

S. van der Linden[1] · R. Hagmeijer[2] · G. R. B. E. Römer[1]

Received: 7 August 2023 / Accepted: 6 October 2023 / Published online: 6 November 2023

Abstract
Under water laser ablation is a surface texturization method used to form micrometer-sized surface structures. Plasma confinement and cavitation bubble evolution play a critical role during the ablation process and their influence on material removal is strongly tied to liquid layer thickness. To influence the effects of these processes, such that material removal is at its maximum, an optimal layer thickness was found for various laser parameters. Specifically, for nanosecond pulsed laser ablation of stainless steel, however, the relation between layer thickness and volume removal is still unknown. Here, we show the relation between water layer thickness and removed material volume for a nanosecond pulsed laser. Results reveal that volume removal is at its maximum for a 1 mm water layer and drops by a factor of 2 when the layer thickness is increased to 2 mm. A further increase of layer thickness to 3 up to 10 mm shows a negligible effect on volume removal and removed volume amounts are shown to be similar to those obtained in ambient air in this water layer thickness range. This trend echo's results obtained for nanosecond pulsed silicon ablation. The obtained results identify processing conditions which allow for faster and therefore more cost efficient texturization of stainless steel surfaces in the future.

Keywords Ablation · Water · Air · Laser · Nanosecond · Stainless steel

1 Introduction

Pulsed laser processing is a versatile material processing technique which has found application fields in the form of thin film deposition [1], surface peening [2] and cladding [3]. In addition, pulsed laser ablation is by now a well-known method by which microscopic (blind) holes can be drilled in various materials [4]. Within this category of pulsed laser processing, under water pulsed laser ablation is currently a topic of active research for the production of nanoparticles [5] used for, e.g., medical purposes [6]. The method is also used to create nanostructures [7] and surface modifications on a nanometer scale [8]. Specifically, for stainless steel, pulsed laser ablation has been used to alter the hydrophobic properties of stainless steel surfaces [9, 10] and to create trenches [11]. In the context of under water pulsed laser ablation, stainless steel was ablated in the past to create stents [12] and surface microtextures [13]. Reasons for ablating under a liquid layer include: craters shot under water are reported to be deeper than their in air ablated counter parts [14], contain less redeposited material and are therefore "cleaner" [15, 16]. Significant crater taper differences between ablation in air and ablation under water were also reported [17]. Changing liquid layer thickness above the ablated sample can have a significant impact on crater depth, though literature shows varying ideal thicknesses to ablate the most volume per laser pulse. On silicon, a 1 mm water layer was shown to be optimal [18], and for polymethylmethacrylate, a 500 µm layer creates deepest craters [19]. Under water ablation on Inconel 718 was performed for different liquid layer thicknesses after which it was concluded that thinner liquid layers result in deeper craters, whereas thicker liquid layers cause a crater widening at the cost of shallower holes [20]. Aforementioned results indicate a thinner liquid layer is most beneficial. For aluminum, however, it was found that a 3 mm water layer created deepest surface structures [21]. Analysis of plasma and cavitation bubble

✉ S. van der Linden
s.vanderlinden@utwente.nl

[1] Department of Mechanics of Solids, Surfaces and Systems, University of Twente, Drienerlolaan 5, 7522 NB Enschede, The Netherlands

[2] Department of Engineering Fluid Dynamics, University of Twente, Drienerlolaan 5, 7522 NB Enschede, The Netherlands

dynamics in the pulsed laser ablation under water process have shown that ablation occurs most efficiently when the liquid layer thickness is set close to, but larger than plasma and cavitation bubble spatial dimensions [22]. Dimensions of both plasma and the cavitation bubble were identified in the past for various ablation conditions [23–27] and plasma and cavitation bubble evolution is documented [28, 29] as well. Plasma emission time under a water layer may be shorter than the plasma emission time for a plasma created in ambient air by an order of magnitude due to the heat conductivity of water being higher than that of air [30]. Relative to plasma created in ambient air, the underwater created plasma region over which emission is visible is decreased by an order of magnitude too [31]. The transition from plasma to cavitation bubble typically occurs after several hundreds to thousands of nanoseconds [28] and during the growth and collapse phases of the cavitation bubble persistent bubbles, that is, bubbles with a lifetime of milliseconds to seconds [32] may be ejected [33] from the cavitation bubble. In addition, nanoparticles are released into the water during cavitation bubble evolution [34]. Although the aforementioned literature studied the under water ablation process in depth, a direct relation between laser pulse energy, sample material and water layer thickness is not presently available. Therefore, the goal of this paper is to explore this relationship for the infrared nanosecond pulsed laser ablation of stainless steel under a demineralized water layer of varying thicknesses.

2 Materials and methods

2.1 Laser and imaging setup

Figure 1 shows the laser set-up used. A 33 ns pulsed fibre laser source (RedEnergy G4 pulsed fibre of SPI Lasers, UK) with a fundamental wavelength of 1060 nm was used for all ablation experiments. The beam quality of this laser source equals $M^2 = 1.06$. The pulse frequency of the laser was set to 1 kHz to avoid interaction of the laser beam with (potential) cavitation bubbles. The laser beam was attenuated by means of a $\lambda/2$-plate and a polarizing beam splitter to set power output accurately. The laser beam was then focussed using an F-theta telecentric lens (F-theta-Ronar lens by Linos AG, Germany) with a focal length of 80 mm mounted on a Galvo-scanner (intelliScan 14 of Scanlab, Germany). The F-theta telecentric lens focussed the laser beam into an optically transparent watertight box. The diameter of the laser focus was measured to be 24 ± 0.5 µm outside of the box using a beam profiler (MicroSpotMonitor by Primes, Germany). Linear stages (ATS150 of aerotech, USA) were used to align the box with the Galvo-scanner. The box itself was mounted on an *xy*-stage system (two ALS20020 stages of Aerotech, USA) to allow spatial manipulation of the box with respect to the laser beam. Epoxy embedded sample material was mounted inside the box by means of two gauge blocks with identical thicknesses. The thickness tolerance on the gauge blocks was better than 1 µm. Gauge blocks and sample were fastened (i.e. clamped to the box) using magnets. The box itself was used in prior experiments [35] and consisted of 4 optically transparent, visible light anti-reflective coated silica glass plates with a width and height of 50 mm and a thickness of 4 mm each. The base plate of the box was made of aluminum. A schematic image and a photograph of the box is shown in Fig. 2. Notice vertical mounting of the sample allows bubbles to escape from the laser targeted area due to buoyancy. Laser power measurements were made in front of the optically transparent box by means of a power meter (FieldMax II-To of Coherent, USA) and a power sensor (P10 of Coherent, USA).

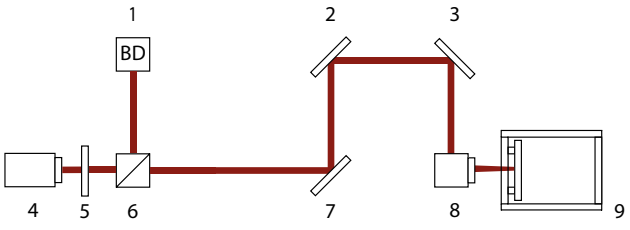

Fig. 1 Schematic of the used set-up. Numbers denote: 1: beam dump, 2, 3 and 7: mirrors, 4: laser source, 5: 1/2λ-plate, 6: beamsplitter cube, 8: Galvano-scanner, 9: optically transparent watertight box

2.2 Samples

Stainless steel 304 plate samples with a width and height of 20 mm and approximate thickness of 1 mm were embedded into an epoxy and polished to obtain a surface

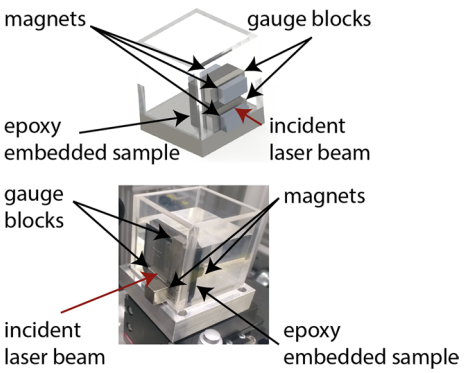

Fig. 2 Top image: Rendered image of the optically transparent, watertight box, including gauge blocks, magnets and epoxy embedded sample. Bottom image: Photograph of the watertight box, notice the gauge block configuration is slightly altered relative to the configuration shown in the rendered image

roughness of Ra 0.18 µm. Under water experiments were facilitated by submerging sample and gauge blocks in demineralized water.

2.3 Ablation conditions, focus shift and effective pulse energy

Ablation tests were performed using 50 consecutive pulses at a 1 kHz laser pulse frequency for 9 different pulse energy levels in ambient air, and under various water layer thicknesses. Prior to running experiments, the focus location was determined on a dummy sample inside the optically transparent box in ambient air. For experiments under water, the focus location in air was compensated with a distance H away from the focusing optics [36]:

$$H = h_l(1 - 1/n_{\text{water}}), \tag{1}$$

in which h_l is the water layer thickness and n_{water} is the refractive index of water, $n_{\text{water}} = 1.330$ [37]. To compare ambient air and ambient water results, effective pulse energies on the sample surface are computed. This method is used to compensate for medium and sample surface reflectivity [35, 38] for ultra-short pulsed laser ablation. In the case of ultra-short pulsed laser ablation, lattice heating takes place after the laser pulse has hit the sample whereas for nanosecond laser ablation, lattice excitation and laser-material interaction occur (partly) simultaneously [39]. As the refractive index of a material tends to be strongly temperature dependent (silicon [40] and silver [41] are excellent examples of this trend), reflections at the ambient-stainless steel interface are not taken into account in the effective energy computation in our work. Hence, only losses at the air/transparent box and at the transparent box/ablation ambient interface are taken into account. Transmission values for ambient air and water experiments are provided in Table 1 based on the refractive index of air (1.000 [42]), water (1.330 [37]) and the fused silica used as optically transparent walls of the transparent and watertight box (1.462 [43]).

Using the transmission values of Table 1, the effective pulse energy was varied from 63.1 to 142 µJ in ambient air and from 65.2 to 147 µJ under water.

Table 1 Transmission values for stainless steel ablated in ambient air and water within the optically transparent box

Ambient	Transmission values
T_{air}	0.934
T_{water}	0.964

2.4 Crater volume analysis: thresholds

Traditionally, threshold fluences are used to identify the onset of laser induced surface modification and both area [44] and volume methods [45, 46] were presented to identify these fluences. These procedures share the assumption that the laser fluence profile is Gaussian on the sample surface. To satisfy this condition the ambient in which the laser propagates prior to hitting the sample must remain reasonably homogeneous. However, under water ablation gives rise to bubbles which may linger in the vicinity of the ablation area [32]. These bubbles may obstruct the beampath, creating an inhomogeneous medium for the laser to traverse. As such, material deformation is not identified by means of threshold fluences, but rather identified on a pulse energy basis.

2.5 Crater volume analysis: method

Nanosecond pulsed laser ablation may give rise to not just crater, but also rim formation around the crater perimeter [47]. The volume associated with these rims is typically disregarded but here these will be taken into account to determine the amount of material removal associated with craters. The adopted method to extract crater volumes is identical to the one proposed in earlier work [48]. A method to identify rim volumes and removed volumes is provided in this section.

Craters are analysed by means of light microscopy as well as confocal laser scanning microscopy (CLSM, VK-9710 of Keyence, Japan). A 1024×768 pixel camera was used to create images of each individual crater. The 1-σ repeatability error of the confocal microscope is 0.02 µm. Interpret the pixels covering a crater filled confocal image as N quadrilateral cells with cell centered altitudes z_i and coordinates x_i and y_i and area ΔA. The cells are categorized in a band region Ω_{b} and a middle region Ω_m with number of elements N_{b} in the band region, see Fig. 3.

Using the method described in our earlier work [48], the equivalent crater diameter d_{c} and crater volume V_{c} are computed based on the number of band elements N_{b} the accepted relative error in the number of crater elements β_{c} and the number of smoothing iterations n_{s}. Quantification of all crater related parameters are provided in the appendix. To quantify rim volumes around the crater edge, define a hump threshold $\tilde{z}_{\text{h}}^{\star}$ above which tilt compensated altitude data points $\tilde{z}_i$ count towards the total number of hump elements N_{h}. An estimate for N_{h} is expressed as

$$N_{\text{h}} = \delta N_{\text{s}}, \quad 0 < \delta < 1, \tag{2}$$

in which δ is a proportionality constant and N_{s} is the number of cells covered by the size of the laser spot. The error of this estimate, ΔN_{h}, is equal to the number of improper hump

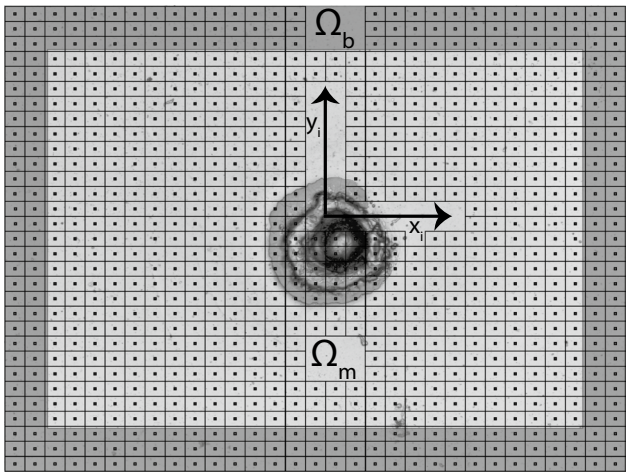

Fig. 3 Schematic depiction of region Ω, band region Ω_b and middle region Ω_m covered by quadrilateral cells each with its own center point. Coordinates y_i and x_i are also indicated and the image in the background is an underwater ablated crater shown solely for illustrative purposes. The number of quadrilateral cells visible is not representative for the total number of cells used in subsequent computations

elements positioned outside of the estimated hump region, and reads

$$\Delta N_\mathrm{h} = \gamma(N - N_\mathrm{h} - N_\mathrm{c}). \tag{3}$$

In (3), γ is the fraction of improper hump elements within an unprocessed region and N_c denotes the number of crater elements. In accordance with prior work [48], N_c is assumed to be approximately equal to N_s. The relative error β_h in N_h is then equal to

$$\beta_\mathrm{h} \equiv \frac{\Delta N_\mathrm{h}}{N_\mathrm{h}} \approx \frac{\gamma}{\delta}\left(\frac{N}{N_\mathrm{s}} - 1 - \delta\right). \tag{4}$$

A single value of γ is obtained by choosing a single value of δ. In the next subsection it will be shown that an appropriate value of δ is 1, simplifying (4) to

$$\beta_\mathrm{h} \approx \gamma\left(\frac{N}{N_\mathrm{s}} - 2\right). \tag{5}$$

Each value of γ is coupled to a single value of the threshold $\tilde{z}_h^\star$ obtained from unablated sample material. This threshold value is then used as the reference altitude above which elements are considered hump elements in the analysis of all confocal images of ablated regions. With the hump threshold defined, N_h may be computed for every crater and the hump volume V_h is then determined as

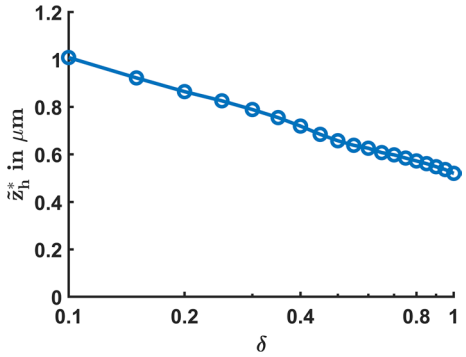

Fig. 4 Hump threshold $\tilde{z}_h^\star$ as a function of δ, computed off of unablated confocal data, $\beta_\mathrm{h} = 0.01, N/N_\mathrm{b} = 0.1$

$$V_\mathrm{h} = \left(\sum_{i \in I_\mathrm{h}} \tilde{z}_i\right)\Delta A, \tag{6}$$

in which I_h are the indices belonging to all hump cells. The total removed volume V is then computed based on the crater volume V_c and the hump volume V_h as

$$V = V_\mathrm{c} - V_\mathrm{h}. \tag{7}$$

2.6 Crater volume analysis: parameter validation

To compute V_h and V, two parameters must be defined in addition to the parameters used in defining V_c. These two parameters are

1. the acceptable relative error in the number of hump points, β_h,
2. a suitable scaling factor δ.

A value of $\beta_\mathrm{h} = 0.01$ was deemed adequate for the analysis of all analysed data. In the pursuit of finding a suitable value for δ in Eq. (2), a range of δ values is considered between 0.1 and 1 for each of which a γ value is computed. The hump thresholds $\tilde{z}_\mathrm{h}^\star$ corresponding to each of the computed γ values is shown as a function of δ for unprocessed sample material in Fig. 4.

To determine which δ value corresponds to an appropriate threshold $\tilde{z}_h^\star$ for the hump analysis, the sensitivity of $\langle N_\mathrm{h}\rangle$, the pulse energy averaged number of hump elements for all craters, to changes in δ is determined by computing $\langle N_\mathrm{h}\rangle$ for the δ values considered in Fig. 4. The outcome of this analysis is shown in Fig. 5.

Figure 5 shows that $\langle N_\mathrm{h}\rangle$ steadily increases for increasing values of δ for all ambients. This steady increase signifies a minimal contribution of unablated area to N_h over the entire range of δ. Therefore, $\delta = 1$ is selected for all subsequent crater hump analysis as this value maximizes the number of true

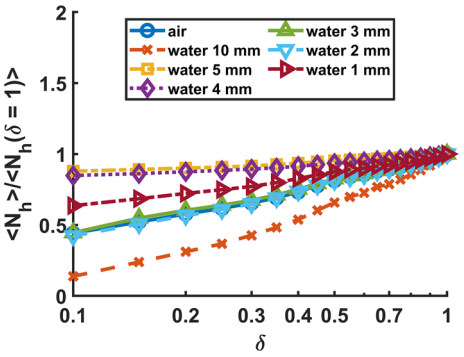

Fig. 5 The pulse energy averaged number of hump elements for all craters, $\langle N_h \rangle$, as a function of δ for crater data in all different ambients. Presented results are scaled using $\langle N_h \rangle$ at $\delta = 1$, $\beta_h = 0.01$, $N/N_b = 0.01$, $n_s = 10$ for 1-mm water layer results, 0 for all other ambients

hump elements while contributions of the unablated surface are suppressed as much as for any other δ value within the considered range of δ. Based on Fig. 4, this amounts to a hump threshold of $\tilde{z}_h^\star = 0.4874\,\mu m$.

To quantify the error made in obtaining V, the removed volume for 10 unablated confocal images is computed. As the laser ablated volume for these images is 0 by definition, The computed removed volume values for these images serve as a reliable error estimate. Results of this procedure are provided in Table 2. Note that the presented results allow for negative removed volumes.

3 Results

3.1 Volume results

Figure 6 shows the crater, hump and removed volumes as a function of pulse energy.

Combining the information in these graphs, it is evident that:

- Crater and hump volume start significantly increasing at an energy threshold of 110 µJ, regardless of ambient (air, water).
- The pulse energy threshold at which volume is actually removed, that is, $V > 0$, varies with ambient and layer thickness and is typically higher than the energy threshold for which crater V_c and hump V_h volumes start increasing. This implies that, for these low pulse energies, the material of the crater is predominantly "pushed" into the rim, rather than removed from the material for these low pulse energies.
- Crater and hump volume are strongly ambient and water layer thickness dependent; these volumes are highest for a 1 mm water layer, whereas for increasing water layer thicknesses crater and hump volume strongly decrease until it is at about the level of ambient air for a 10 mm water layer.

Table 2 Removed volume data obtained for 10 unablated stainless steel confocal images

Mean standard deviation removed volume (μm^3)	Removed volume (μm^3)
50.78	122.2

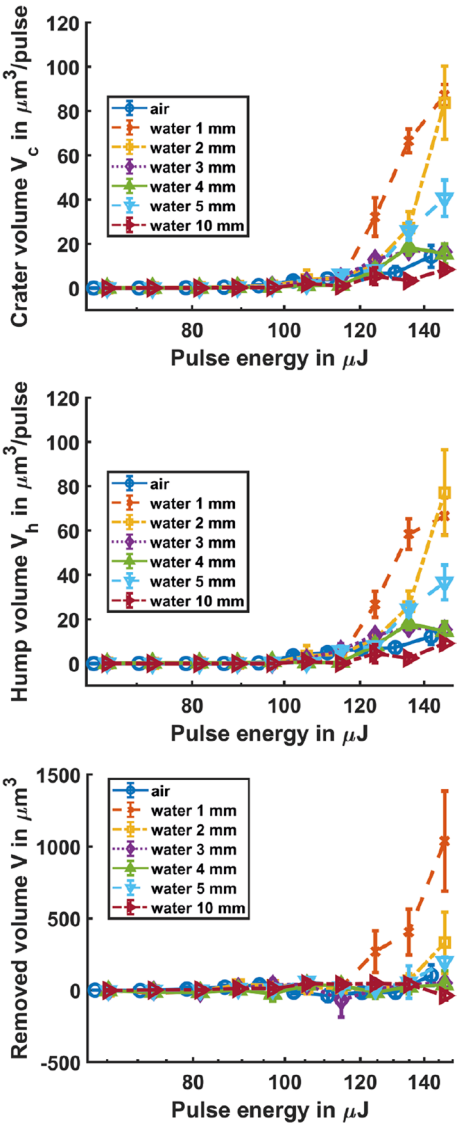

Fig. 6 Crater, hump and removed volumes as a function of pulse energy, $\beta_c = \beta_h = 0.01$, $N_b/N = 0.1$, $\delta = 1$, $n_s = 10$ for 1-mm water layer results, 0 for all other ambients

The ambient independence of the crater and hump volume energy threshold indicates that this threshold is a laser-material dependent property, whereas the volume removal energy threshold depends also on ambient conditions. For results obtained under a 1 mm water layer, the volume removal threshold is equal to the crater and hump volume energy threshold whereas the volume removal energy threshold is about 115 µJ for a 1 mm water layer, 125 µJ for a 2 mm water layer, 135 µJ for a 5 mm water layer and 130 µJ in ambient air. For all other considered ambients, this threshold does not seem to exist as an insignificant amount of volume is removed over the considered pulse energy range. This lack of ablated volume and presence of hump and crater volumes suggests material displacement rather than evaporation or ionisation to be the dominant factor in the formation of the crater. It is known that vapor and plasma plumes created during the ablation process cause significant pressure gradients in and above the sample material [31, 49, 50], which cause the volume displacement. Note that the absence of ablated volume does not imply no material evaporation or ionisation occurred; it merely indicates that the material removed is too small to quantify. The ablated volume dependence on water layer thickness is consistent with earlier findings [18], though the reported layer thickness sensitivity in that article is larger than shown in Fig. 6.

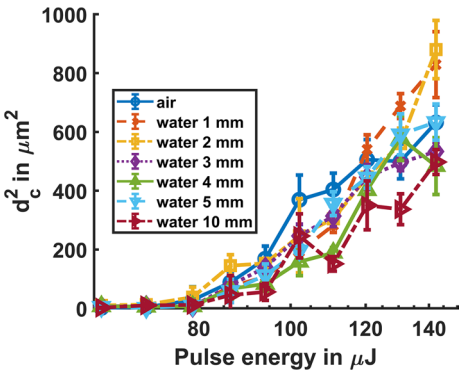

Fig. 7 Crater diameter squared, d_c^2 as a function of pulse energy, $\beta_c = \beta_h = 0.01$, $N_b/N = 0.1$, $\delta = 1$, $n_s = 10$ for 1-mm water layer results, 0 for all other ambients

3.2 Diameter results

The square of the equivalent crater diameter d_c is plotted as a function of pulse energy in Fig. 7. This variable is of interest as it is a measure for the area that a crater covers. Contrary to results obtained using a picosecond pulsed laser source [35], Fig. 7 shows a largely ambient independent trend of the crater diameter. This trend indicates d_c^2 values steadily increase starting at a threshold of 80 µJ, with the largest rate of increase observed for a 1 mm and 2 mm water layer and a lower increase for all other ambient conditions. For pulse energies below the threshold value, the squared equivalent diameters are nearly zero, indicating craters are too shallow for the crater determination method to yield sensible results. Interestingly, the defined d_c^2 energy threshold lies 20 µJ lower than the displaced volume threshold identified in the previous paragraph. This means that for craters created using pulse energies between the d_c^2 energy threshold and the displacement volume threshold, craters are characterised by a very shallow depth relative to the surface roughness of the sample. It also signifies that in this pulse energy regime, crater size increase is predominantly caused by an increase in crater area rather than depth.

3.3 Threshold identification

Summarising the volume and equivalent diameter analysis, the material response to incident laser pulses may be characterised by three thresholds (see also Table 3):

- A surface modification threshold E_s, below which area and volume modifications are not distinguishable from surface roughness characteristics.
- A displaced volume threshold E_d, below which a negligible amount of volume is displaced and above which volume modifications are characterised by displacement of material from the crater to the rim but not by material removal.
- A removed volume threshold E_r, below which a negligible amount of volume is removed and above which laser irradiated regions are characterised by non-zero crater volume.

Table 3 Energy thresholds

Threshold name	Symbol	Value (range) (µJ)	Ambient
Surface modification threshold	E_s	80	All
Displaced volume threshold	E_d	110	All
Removed volume threshold	E_r	115–135	Air, 1, 2 and 5 mm water layer

Out of these three thresholds, E_s and E_d are ambient independent, i.e. laser-material dependent properties and E_r is ambient dependent and only exists within the considered pulse energy range for a select few ambients. A quantification of these thresholds and the ambient for which they are applicable is listed in Table 3.

Note that the listed thresholds in Table 3 are not meant to signify the onset of surface modifications in general. Instead, they identify pulse energy regimes below and above which surface roughness compensated crater characteristics change significantly.

3.4 Crater morphology

Light microscopy images of a selected number of craters are shown in Fig. 8. A filled contour overlay was placed over the light microscopy images to identify altitude variations in the image. Cross-sections, of the craters shown in Fig. 8, are displayed in Fig. 9. The cross-sectional data are scaled using the crater threshold, $\tilde{z}_c^\star$ and reference lines for the crater and hump energy thresholds are included in the graphs.

The first column in Fig. 8 demonstrates the influence of the hump and crater thresholds; even though optically a significant region of the laser illuminated sections are modified, only a very small portion of these regions is deep(crater) or high(hump) enough to contribute to crater or hump volume as indicated by the tiny blue colored sections. In the second column i.e. at higher pulse energies, small rims can be observed at the outer edge of the ablated region for the craters created in air and under a 10-mm water layer. Although in air ablated craters are distinctly darker coloured (in Fig. 8) than the under water ablated craters, differences between the ambients in terms of altitude are not that significant for these first two columns. Starting at the third column though, the effect of the ambient differences become very clear as the results obtained for 1 and 5 mm water show significantly higher rims and deeper craters than the results for the other ambients.

The influence of the hump and crater thresholds is shown graphically in Fig. 9; even though surface modifications are clearly present in the cross-sections in the first column, only a very small fraction of the modifications are actually significant enough to pass above the hump threshold or below

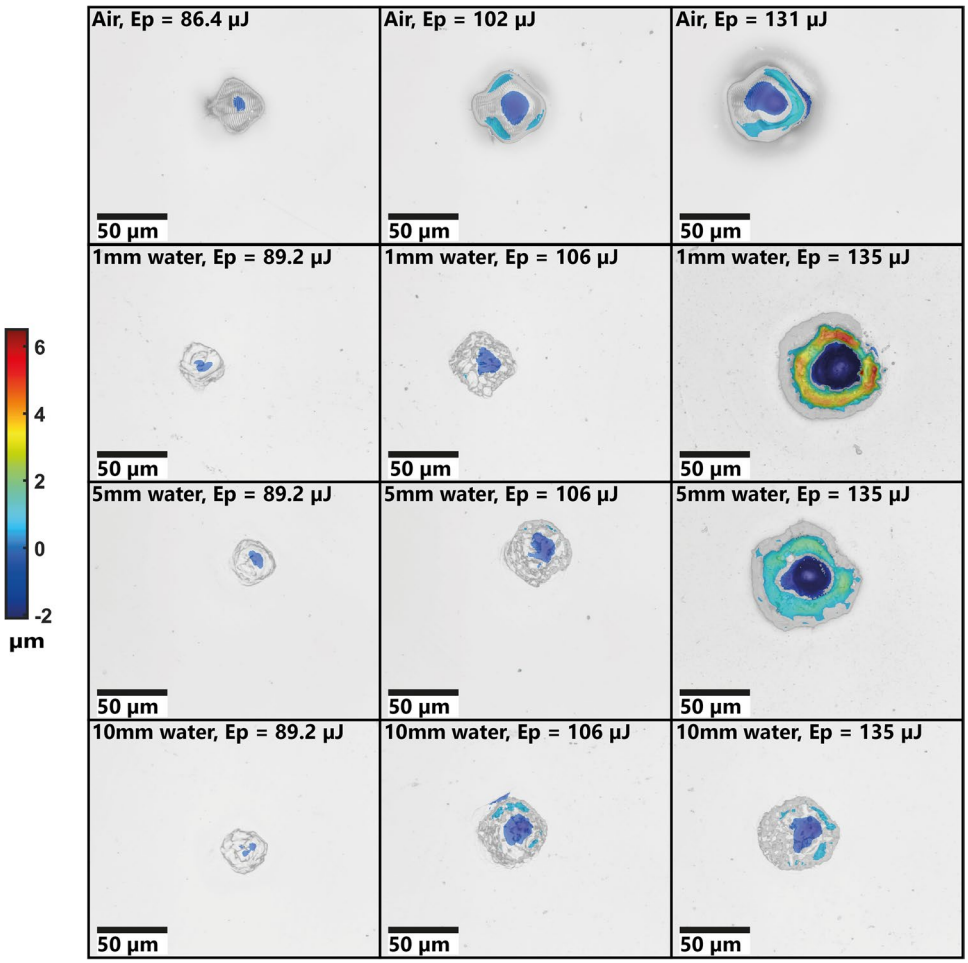

Fig. 8 Filled contour height plots combined with black and white optical microscopy images of selected ambient and pulse energies. 196 contour levels were used in the creation of the contour images. $\beta_c = \beta_h = 0.01, N_b/N = 0.1, \delta = 1, n_s = 10$ for 1-mm water layer results, 0 for all other ambients. The colorbar indicates altitudes in µm

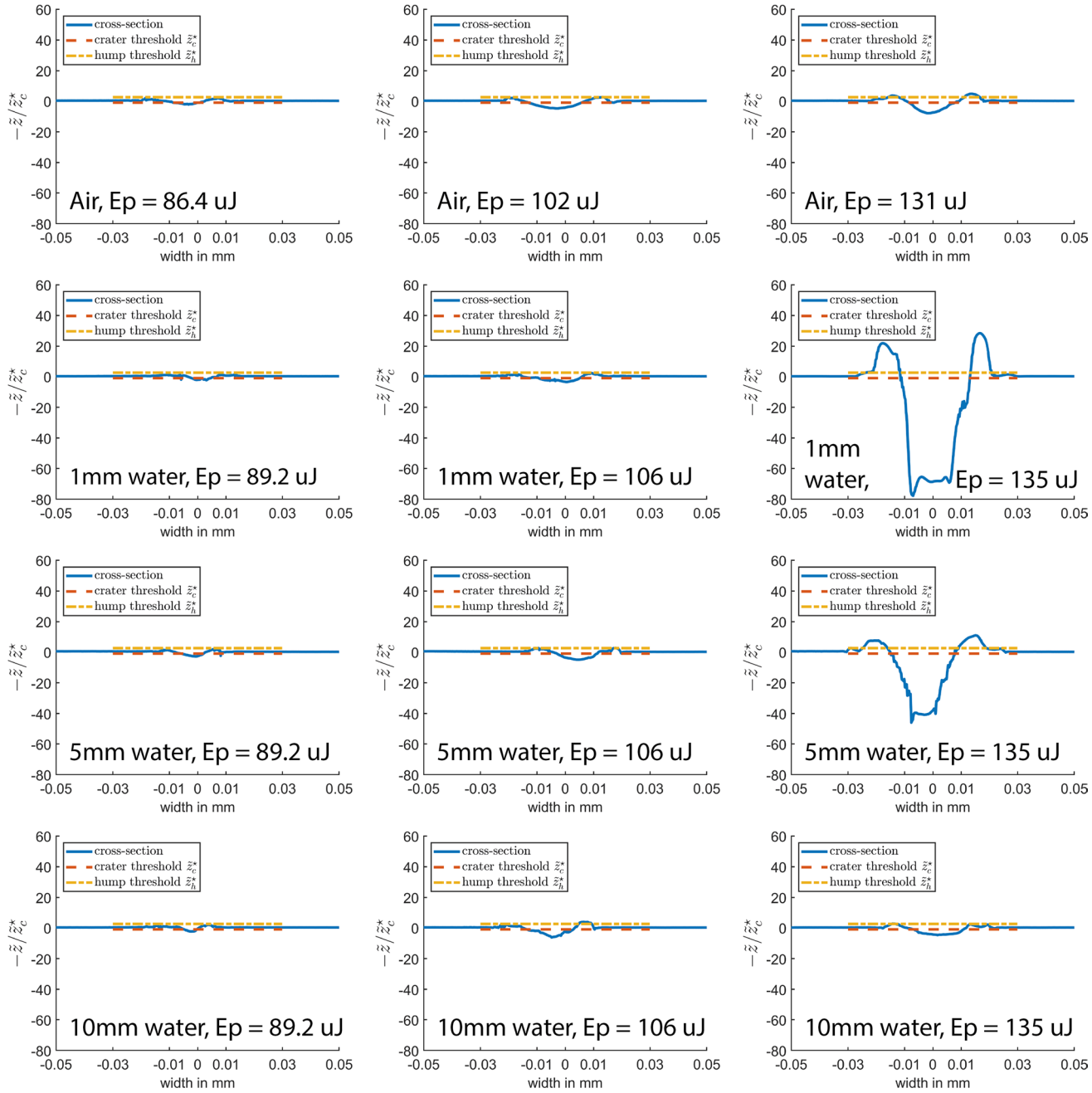

Fig. 9 Crater cross-sectional areas for selected ambient and pulse energies, along with crater $\tilde{z}_c^\star$ and hump $\tilde{z}_h^\star$ thresholds. $\beta_c = \beta_h = 0.01$, $N_b/N = 0.1, \delta = 1, n_s = 10$ for 1-mm water layer results, 0 for all other ambients

the crater threshold. Interestingly, in air and under a 10 mm water layer ablated craters show a very gentle slope over the cross-sectional width of the crater, whereas for the ablated areas created under a 1 and 5 mm water layer, the first two columns show a gently sloping cross-section and sharp surface gradients for the craters in the third column. This radical slope change is reminiscent of similar behaviour shown in aluminum [51]. The cross-sections show that crater depth increase rather than width increase is the most dominant reason for volume increase as pulse energy is increased, this is consistent with earlier reports [14].

3.5 Influence of water layer thickness on the ablation process

Clearly the optimal layer thickness, that is, the water layer thickness for which most material is removed, is a layer of 1 mm and the amount of removed material strongly

decreases to levels comparable to those obtained in ambient air for increasing layer thicknesses. It is known that plasma formation and cavitation bubble evolution in the ablation process under a water layer give rise to shockwave propagation [27, 28]. Prior work on water layers with an air free surface indicates that these shockwaves are effectively backreflected off of the free surface onto the original ablation zone above a certain layer thickness threshold, which causes an increase in mechanical stress in the target material [52]. These backreflections were noted to be the reason for an ablation efficiency increase [22] relative to layer thicknesses below this threshold. For the studied conditions in the relevant works, layer thickness thresholds were found to lie in the 0.8–1 mm range, [52] which corresponds decently with results provided in the presented work. Although the water layer in the presented work is subject to a rigid fused silica boundary rather than an air free surface, the back reflected shockwaves are still believed to cause the sharp increase in ablated volume at a water layer of 1 mm. The sharp decrease in ablated volume observed for water layer thicknesses of multiple millimeters was observed in other works too [19], which was explained by the reduction of reflected shockwave strength [21].

4 Conclusions

Nanosecond pulsed laser ablation of stainless steel using an infrared laser source was performed in ambient air and under varying water layer thicknesses. Existing theory on the analysis of crater volume was used and expanded to include crater hump volume (volume of rim around the laser induced crater). Using this expanded analysis method, pulse energy ranges in which surface modification, volume displacement and volume removal took place were identified. For effective laser pulse energies between 80 and 110 µJ, crater volume changes consisted mostly of material displacement to the crater rim. Significant volume removal was found to occur above an ambient specific energy threshold and ranged from 115 to 135 µJ. Volume removal was highest for ablation performed under a 1 mm water layer which was attributed to shockwave backreflections onto the ablation zone on the sample. With an increase in water layer thickness the volume of the craters rapidly decreased. Rim structures were found to occur on the edges of craters formed under water as well as in ambient air. Finally, crater volume increase was attributed primarily to an increase in crater depth, not width. Note that the aforementioned conclusions strictly relate to single crater ablation. For more complex structures, such as grooves, the influence of persistent bubbles is expected to have a detrimental effect on crater volume.

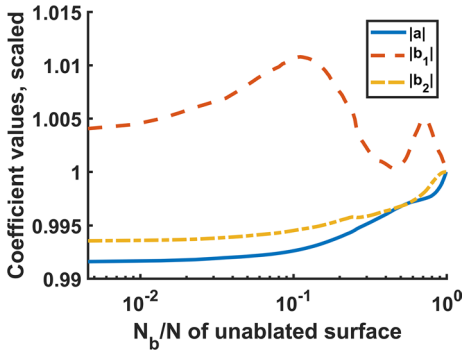

Fig. 10 Absolute linear surface coefficients of equation as a function of N_b/N for an unablated sample, scaled to their values at $N_b/N = 1$

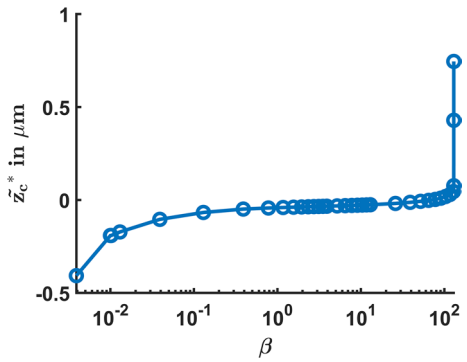

Fig. 11 $\tilde{z}_c^\star$ as a function of β for unablated sample material, $N_b/N = 0.1$

Appendix: Crater parameters

To determine the number of crater elements N_c, crater volumes V_c and equivalent diameters d_c, a linear tilt compensation function must be defined as well as a crater threshold altitude $\tilde{z}_c^\star$ and the number of smoothing iterations n_s [48]. The tilt compensation function coefficients a, b_1 and b_2, are recomputed for every crater image containing N elements based on the number of band elements N_b. The number of band elements is determined based on coefficient behaviour as a function of N_b for an unablated sample as shown in Fig. 10. Based on this graph, $N_b/N = 0.1$ is chosen for the crater analysis.

To define $\tilde{z}_c^\star$, the acceptable relative error in the number of crater points β_c is chosen equal to 0.01. The corresponding threshold is determined from Fig. 11 and is equal to –0.1909 µm.

Craters induced by a pulse energy of 106 µJ or more under a 1 mm water layer suffer from substantial surface gradient induced noise. To analyse the effect of smoothing iterations on this crater set, craters created using 106, 124 and 147 µJ under a 1 mm water layer are displayed

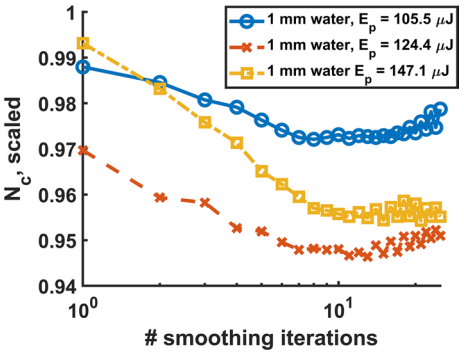

Fig. 12 Number of crater elements N_c as a function of number of filter iterations n_s for craters created using three different pulse energy levels under a 1 mm water layer. The number of crater elements is scaled using the non-smoothened number of crater elements

in Fig. 12. As can be observed in this figure, N_c values appear largely stable for 10 smoothing iterations or more. Therefore, all craters shot under a 1 mm water layer for 106 µJ or more are subjected to $n_s = 10$ smoothing iterations. All other crater data was found to be noise free and thus requires no smoothing.

Defining n_s completes the crater parameter identification and thus N_c, V_c and d_c may be computed for every crater image.

Author contributions SvdL: conceptualization (equal); data curation (lead); formal analysis (equal); methodology (equal); software (lead); validation (equal); visualization (lead); writing-original draft preparation (lead). RH: conceptualization (equal); formal analysis (equal); funding acquisition (equal); methodology (equal); project administration (equal); resources (equal); software (equal); supervision (equal); validation (equal); writing-review and editing (equal). GRBER: conceptualization (equal); formal analysis (equal); funding acquisition (equal); methodology (equal); project administration (equal); resources (equal); software (equal); supervision (equal); validation (equal); writing-review and editing (equal).

Funding This study was funded by the European INTERREG project "Safe and Amplified Industrial Laser Processing" (SailPro), as part of the "RegiOnal Collaboration on Key Enabling Technologies" (ROCKET),http://www.rocket-innovations.eu.

Availability of data and materials Data available on request from the authors.

Declarations

Conflict of interest The authors declare that they have no known competing financial interests or personal relationships that could have appeared to influence the work reported in this paper.

References

1. M. Ashfold, F. Claeyssens, G. Fuge, S. Henley, Pulsed laser ablation and deposition of thin films. Chem. Soc. Rev. **33**(December 2004), 23–31 (2004). https://doi.org/10.1039/b207644f
2. A.K. Gujba, M. Medraj, Laser peening process and its impact on materials properties in comparison with shot peening and ultrasonic impact peening. Materials **7**(12), 7925–7974 (2014). https://doi.org/10.3390/ma7127925
3. C.P. Paul, H. Alemohammad, E. Toyserkani, A. Khajepour, S. Corbin, Cladding of WC-12 Co on low carbon steel using a pulsed Nd:YAG laser. Mater. Sci. Eng. A **464**(1–2), 170–176 (2007). https://doi.org/10.1016/j.msea.2007.01.132
4. M.C. Gower, Industrial applications of pulsed laser micromachining, in *Proceedings of the Conference on Lasers and Electro-Optics Europe—Technical Digest*, vol. 7, no. 2 (1998), p. 247. https://doi.org/10.1109/cleoe.1998.719333
5. B. Gökce, V. Amendola, S. Barcikowski, Opportunities and challenges for laser synthesis of colloids. ChemPhysChem **18**(9), 983–985 (2017). https://doi.org/10.1002/cphc.201700310
6. S.Y. Shim, D.K. Lim, J.M. Nam, Ultrasensitive optical biodiagnostic methods using metallic nanoparticles. Nanomedicine **3**(2), 215–232 (2008). https://doi.org/10.2217/17435889.3.2.215
7. H. Liu, F. Chen, X. Wang, Q. Yang, H. Bian, J. Si, X. Hou, Influence of liquid environments on femtosecond laser ablation of silicon. Thin Solid Films **518**(18), 5188–5194 (2010). https://doi.org/10.1016/j.tsf.2010.04.043
8. D. Zhang, B. Ranjan, T. Tanaka, K. Sugioka, Underwater persistent bubble-assisted femtosecond laser ablation for hierarchical micro/nanostructuring. Int. J. Extrem. Manuf. **2**(1), 015001 (2020). https://doi.org/10.1088/2631-7990/ab729f
9. Y. Cai, W. Chang, X. Luo, A.M. Sousa, K.H.A. Lau, Y. Qin, Superhydrophobic structures on 316L stainless steel surfaces machined by nanosecond pulsed laser. Precis. Eng. **52**(October 2017), 266–275 (2018). https://doi.org/10.1016/j.precisioneng.2018.01.004
10. P. Pou, J. del Val, A. Riveiro, R. Comesaña, F. Arias-González, F. Lusquiños, M. Bountinguiza, F. Quintero, J. Pou, Laser texturing of stainless steel under different processing atmospheres: from superhydrophilic to superhydrophobic surfaces. Appl. Surf. Sci. **475**(September 2018), 896–905 (2019). https://doi.org/10.1016/j.apsusc.2018.12.248
11. P. Deladurantaye, D. Gay, A. Cournoyer, V. Roy, B. Labranche, M. Levesque, Y. Taillon, Material micromachining using a pulsed fiber laser platform with fine temporal nanosecond pulse shaping capability. Fiber Lasers VI: Technol. Syst. Appl. **7195**(February 2009), 71951S (2009). https://doi.org/10.1117/12.809532
12. N. Muhammad, D. Whitehead, A. Boor, L. Li, Comparison of dry and wet fibre laser profile cutting of thin 316L stainless steel tubes for medical device applications. J. Mater. Process.

Technol. **210**(15), 2261–2267 (2010). https://doi.org/10.1016/j.jmatprotec.2010.08.015
13. Y. Ye, M. Wu, X. Ren, J. Zhou, L. Li, Hole-like surface morphologies on the stainless steel surface through laser surface texturing underwater. Appl. Surf. Sci. **462**(May), 847–855 (2018). https://doi.org/10.1016/j.apsusc.2018.08.117
14. S. Zhu, Y.F. Lu, M.H. Hong, X.Y. Chen, Laser ablation of solid substrates in water and ambient air. J. Appl. Phys. **89**(4), 2400–2403 (2001). https://doi.org/10.1063/1.1342200
15. W. Feng, J. Guo, W. Yan, Y.C. Wan, H. Zheng, Deep channel fabrication on copper by multi-scan underwater laser machining. Opt. Laser Technol. **111**(September 2018), 653–663 (2019). https://doi.org/10.1016/j.optlastec.2018.10.046
16. V. Tangwarodomnukun, H.Y. Chen, Laser ablation of PMMA in air, water, and ethanol environments. Mater. Manuf. Process. **30**(5), 685–691 (2015). https://doi.org/10.1080/10426914.2014.994774
17. Q. Chen, H.J. Wang, D.T. Lin, F. Zuo, Z.X. Zhao, H.T. Lin, Characterization of hole taper in laser drilling of silicon nitride ceramic under water. Ceram. Int. **44**(11), 13449–13452 (2018). https://doi.org/10.1016/j.ceramint.2018.04.173
18. S. Zhu, Y.F. Lu, M.H. Hong, Laser ablation of solid substrates in a water-confined environment. Appl. Phys. Lett. **79**(9), 1396–1398 (2001). https://doi.org/10.1063/1.1400086
19. H.W. Kang, A.J. Welch, Effect of liquid thickness on laser ablation efficiency. J. Appl. Phys. (2007). https://doi.org/10.1063/1.2715746
20. J. Lv, X. Dong, K. Wang, W. Duan, Z. Fan, X. Mei, Study on process and mechanism of laser drilling in water and air. Int. J. Adv. Manuf. Technol. **86**(5–8), 1443–1451 (2016). https://doi.org/10.1007/s00170-015-8279-4
21. N. Krstulović, S. Shannon, R. Stefanuik, C. Fanara, Underwater-laser drilling of aluminum. Int. J. Adv. Manuf. Technol. **69**(5–8), 1765–1773 (2013). https://doi.org/10.1007/s00170-013-5141-4
22. M. Dell'Aglio, A. De Giacomo, S. Kohsakowski, S. Barcikowski, P. Wagener, A. Santagata, Pulsed laser ablation of wire-shaped target in a thin water jet: effects of plasma features and bubble dynamics on the PLAL process. J. Phys. D: Appl. Phys. (2017). https://doi.org/10.1088/1361-6463/aa652a
23. S. Reich, A. Letzel, B. Gökce, A. Menzel, S. Barcikowski, A. Plech, Incubation effect of pre-irradiation on bubble formation and ablation in laser ablation in liquids. ChemPhysChem **20**(8), 1036–1043 (2019). https://doi.org/10.1002/cphc.201900075
24. S. Ibrahimkutty, P. Wagener, T.D.S. Rolo, D. Karpov, A. Menzel, T. Baumbach, S. Barcikowski, A. Plech, A hierarchical view on material formation during pulsed-laser synthesis of nanoparticles in liquid. Sci. Rep. **5**, 1–11 (2015). https://doi.org/10.1038/srep16313
25. K. Sasaki, T. Nakano, W. Soliman, N. Takada, Effect of pressurization on the dynamics of a cavitation bubble induced by liquid-phase laser ablation. Appl. Phys. Express **2**(4), 0465011–0465013 (2009). https://doi.org/10.1143/APEX.2.046501
26. J. Lam, J. Lombard, C. Dujardin, G. Ledoux, S. Merabia, D. Amans, Dynamical study of bubble expansion following laser ablation in liquids. Appl. Phys. Lett. **108**(7), 1–6 (2016). https://doi.org/10.1063/1.4942389
27. R. Tanabe, T.T. Nguyen, T. Sugiura, Y. Ito, Bubble dynamics in metal nanoparticle formation by laser ablation in liquid studied through high-speed laser stroboscopic videography. Appl. Surf. Sci. **351**, 327–331 (2015). https://doi.org/10.1016/j.apsusc.2015.05.030
28. M. Dell'Aglio, R. Gaudiuso, O. De Pascale, A. De Giacomo, Mechanisms and processes of pulsed laser ablation in liquids during nanoparticle production. Appl. Surf. Sci. **348**, 4–9 (2015). https://doi.org/10.1016/j.apsusc.2015.01.082
29. A. Kanitz, M.R. Kalus, E.L. Gurevich, A. Ostendorf, S. Barcikowski, D. Amans, Review on experimental and theoretical investigations of the early stage, femtoseconds to microseconds processes during laser ablation in liquid-phase for the synthesis of colloidal nanoparticles. Plasma Sources Sci. Technol. (2019). https://doi.org/10.1088/1361-6595/ab3dbe
30. B. Thornton, T. Ura, Effects of pressure on the optical emissions observed from solids immersed in water using a single pulse laser. Appl. Phys. Express (2011). https://doi.org/10.1143/APEX.4.022702
31. K. Saito, K. Takatani, T. Sakka, Y.H. Ogata, Observation of the light emitting region produced by pulsed laser irradiation to a solid–liquid interface. Appl. Surf. Sci. **197–198**, 56–60 (2002). https://doi.org/10.1016/S0169-4332(02)00303-3
32. M. Kalus, N. Bärsch, R. Streubel, E. Gökce, S. Barcikowski, B. Gökce, How persistent microbubbles shield nanoparticle productivity in laser synthesis of colloids—quantification of their volume, dwell dynamics, and gas composition. Phys. Chem. Chem. Phys. **19**(10), 7112–7123 (2017). https://doi.org/10.1039/c6cp07011f
33. K. Sasaki, N. Takada, Liquid-phase laser ablation. Pure Appl. Chem. **82**(6), 1317–1327 (2010). https://doi.org/10.1351/PAC-CON-09-10-23
34. C.Y. Shih, R. Streubel, J. Heberle, A. Letzel, M.V. Shugaev, C. Wu, M. Schmidt, B. Gökce, S. Barcikowski, L.V. Zhigilei, Two mechanisms of nanoparticle generation in picosecond laser ablation in liquids: the origin of the bimodal size distribution. Nanoscale **10**(15), 6900–6910 (2018). https://doi.org/10.1039/c7nr08614h
35. S. van der Linden, R. Hagmeijer, G. Römer, Picosecond pulsed laser ablation of liquid covered stainless steel: effect of liquid layer thickness on ablation efficiency. J. Laser Micro Nanoeng. **14**(1), 108–119 (2019). https://doi.org/10.2961/jlmn.2019.01.0018
36. A. Menéndez-Manjón, P. Wagener, S. Barcikowski, Transfer-matrix method for efficient ablation by pulsed laser ablation and nanoparticle generation in liquids. J. Phys. Chem. C **115**(12), 5108–5114 (2011). https://doi.org/10.1021/jp109370q
37. E.D. Palik, *Handbook of Optical Constants of Solids* (Academic Press, Cambridge, 1997). https://doi.org/10.1016/C2009-0-20920-2
38. T.J. Derrien, R. Koter, J. Krüger, S. Höhm, A. Rosenfeld, J. Bonse, Plasmonic formation mechanism of periodic 100-nm-structures upon femtosecond laser irradiation of silicon in water. J. Appl. Phys. (2014). https://doi.org/10.1063/1.4887808
39. B.N. Chichkov, C. Momma, S. Nolte, F. von Alvensleben, A. Tünnermann, Femtosecond, picosecond and nanosecond laser ablation of solids. Appl. Phys. A: Mater. Sci. Process. **63**(2), 109–115 (1996). https://doi.org/10.1007/s003390050359
40. J. Šik, J. Hora, J. Humlíček, Optical functions of silicon at high temperatures. J. Appl. Phys. **84**(11), 6291–6298 (1998). https://doi.org/10.1063/1.368951
41. K. Ujihara, Reflectivity of metals at high temperatures. J. Appl. Phys. **43**(5), 2376–2383 (1972). https://doi.org/10.1063/1.1661506
42. M.J. Weber, *Handbook of Optical Materials* (CRC Press, Boca Raton, 2003)
43. R. Kitamura, L. Pilon, M. Jonasz, Optical constants of silica glass from extreme ultraviolet to far infrared at near room temperature. Appl. Opt. **46**(33), 8118 (2007). https://doi.org/10.1364/AO.46.008118
44. J.M. Liu, Simple technique for measurements of pulsed Gaussian-beam spot sizes. Opt. Lett. **7**(5), 196 (1982). https://doi.org/10.1364/OL.7.000196. arXiv:1011.1669v3
45. G. Račiukaitis, M. Brikas, P. Gečys, B. Voisiat, M. Gedvilas, Use of high repetition rate and high power lasers in microfabrication:

how to keep the efficiency high? J. Laser Micro Nanoeng. **4**(3), 186–191 (2009). https://doi.org/10.2961/jlmn.2009.03.0008
46. B. Neuenschwander, G.F. Bucher, G. Hennig, C. Nussbaum, B. Joss, M. Muralt, S. Zehnder, U.W. Hunziker, P. Schuetz, Processing of dielectric materials and metals with PS laserpulses, in *29th International Congress on Applications of Lasers and Electro-Optics(ICALEO) 2010—Congress Proceedings*, vol. 103 (2010), pp. 1079–1083. https://doi.org/10.2351/1.5062103
47. C. Porneala, D.A. Willis, Time-resolved dynamics of nanosecond laser-induced phase explosion. J. Phys. D: Appl. Phys. (2009). https://doi.org/10.1088/0022-3727/42/15/155503
48. S. van der Linden, R. Hagmeijer, G.R.B.E. Römer, Picosecond pulsed underwater laser ablation of silicon and stainless steel: comparing crater analysis methods and analysing dependence of crater characteristics on water layer thickness. Appl. Surf. Sci. (2021). https://doi.org/10.1016/j.apsusc.2020.148005
49. J.M. Fishburn, M.J. Withford, D.W. Coutts, J.A. Piper, Study of the fluence dependent interplay between laser induced material removal mechanisms in metals: vaporization, melt displacement and melt ejection. Appl. Surf. Sci. **252**(14), 5182–5188 (2006). https://doi.org/10.1016/j.apsusc.2005.07.053
50. T.T. Nguyen, R. Tanabe, Y. Ito, Comparative study of the expansion dynamics of laser-driven plasma and shock wave in in-air and underwater ablation regimes. Opt. Laser Technol. **100**, 21–26 (2018). https://doi.org/10.1016/j.optlastec.2017.09.021
51. G. Cristoforetti, S. Legnaioli, V. Palleschi, E. Tognoni, P.A. Benedetti, Observation of different mass removal regimes during the laser ablation of an aluminium target in air. J. Anal. At. Spectrom. **23**(11), 1518–1528 (2008). https://doi.org/10.1039/b800517f
52. T.T.P. Nguyen, R. Tanabe-Yamagishi, Y. Ito, Impact of liquid layer thickness on the dynamics of nano- to sub-microsecond phenomena of nanosecond pulsed laser ablation in liquid. Appl. Surf. Sci. **470**(October 2018), 250–258 (2019). https://doi.org/10.1016/j.apsusc.2018.10.160